Anisotropic Magnetoresistance of a Classical Antidot Array

M. Tornow, D. Weiss, K. v. Klitzing, and K. Eberl

Max-Planck-Institut für Festkörperforschung, Heisenbergstrasse 1, 70569 Stuttgart, Germany

David J. Bergman and Yakov M. Strelniker

School of Physics and Astronomy, Raymond and Beverly Sackler Faculty of Exact Sciences,
Tel Aviv University, Tel Aviv 69978, Israel

A periodic array of cylindrical voids, embedded in a thin film of n-doped GaAs, displays a pronounced anisotropy of the classical magnetoresistance. For a geometry where the magnetic field lies in the plane of the film, we observe a characteristic dependence on the angle between current and magnetic field. This experimental finding provides a first verification of a recently predicted effect and agrees well with theoretical calculations. The observed anisotropy is due to interactions among current distortions by neighboring voids. [S0031-9007(96)00586-8]

The magnetoresistance in simple metals has been one of the fundamental problems of transport for decades [1]. Much work was devoted to the role of inhomogeneities by investigating, e.g., intentional thickness variations of aluminum bars [2] or voids in indium wires [3] as model inhomogeneities. Related transport studies in semiconductor materials with periodically varying donor concentration [4] or InSb with a random distribution of needle shaped NiSb inclusions [5] revealed angle dependent magnetoresistance properties. This is in contrast to the resistance of a free electron gas realized, for example, in the conduction band of Fermi degenerate n-doped GaAs, which in a nonquantizing magnetic field $\mathbf{B}$ shows essentially no dependence on $\mathbf{B}$. A nonvanishing magnetoresistance will occur when inhomogeneities, such as insulating inclusions, distort the current flow pattern as the current is "rerouted" around the obstacles. Hence, the local current density $\mathbf{J}(\mathbf{r})$ deviates from its mean value $\langle \mathbf{J} \rangle = V^{-1} \int_V \mathbf{J}(\mathbf{r}) \, dV$, taken over the sample volume V. Therefore, the presence of insulating inclusions always increases the total dissipation rate $\int \mathbf{J} \cdot \mathbf{E} \, dV$ (with $\mathbf{E}$ the local electric field), and consequently also the effective resistance, above the corresponding values for the homogeneous system [6]. In general, the distortions of the current density become stronger with increasing $\mathbf{B}$, which results in a positive magnetoresistance [7,8].

Here we address the question how mutual (classical) interactions of current distortions from different inclusions affect the magnetoresistance. For the case of periodically arranged inclusions, such as spheres or cylinders embedded in a host material of different conductivity, detailed calculations have been performed [9]. Those have shown that in the classical conduction regime a distinct anisotropy of the resistance exists with respect to the crystallographic axes of the lattice of inclusions [10,11]. In this Letter we provide a first experimental test of the anticipated effects and also present a simple physical picture of this surprising phenomenon.

As host material we chose a 300 nm thick Si-doped GaAs film grown by molecular beam epitaxy on top of an undoped bulk GaAs layer and a semi-insulating GaAs substrate. With respect to the highly conductive n-doped film, the conductivity of the undoped layer is negligible. At $T = 90$ K, the temperature of the experiment, the host n-GaAs had a carrier density of $n_s = 1.6 \times 10^{18}$ cm^{-3} and a mobility of $\mu = 2500$ cm^2/V s, corresponding to a mean free path l_e of only ≈ 75 nm. In order to perform four point magnetoresistance measurements we fabricated a Hall bar mesa, sketched in Fig. 1(b), by means of optical lithography and standard wet etching. A square array of insulating inclusions was then introduced by drilling cylindrical holes through the 300 nm thick epilayer. These holes, with geometric diameters $2r$ of 110, 220, and 260 nm, and a period of $a = 500$ nm, were created, like antidots, by electron beam lithography and dry-etching techniques [12]. However, in contrast with two-dimensional antidot arrays, here the transport is both *three dimensional* and *diffusive* ($l_e \ll a$). Ballistic effects, which are characteristic of two-dimensional electron-gas-based antidots, are not expected to appear under these conditions. An electron micrograph of our classical antidot array is displayed in Fig. 1(a).

The samples were mounted into a superconducting magnet system such that the magnetic field was in the plane of the n-GaAs film. The experimental setup for measuring the angular dependence of the resistance is illustrated in Fig. 1(b). In the experiment, the entire Hall bar, and therefore the applied current $I_x = Wd\langle J_x \rangle$ (where W and d are width and (effective) film thickness of the sample) is rotated *in situ* by an angle α with respect to $\mathbf{B}$. By measuring the voltage drops V_x and V_y, the resistance components $R_{xx} = V_x/I_x$ and $R_{xy} = V_y/I_x$ were evaluated as a function of α. The resistances are related to the resistivities by the usual relations $R_{xx} = (L/Wd)\rho_{xx}$ and $R_{xy} = \rho_{xy}/d$, with L the sample length.
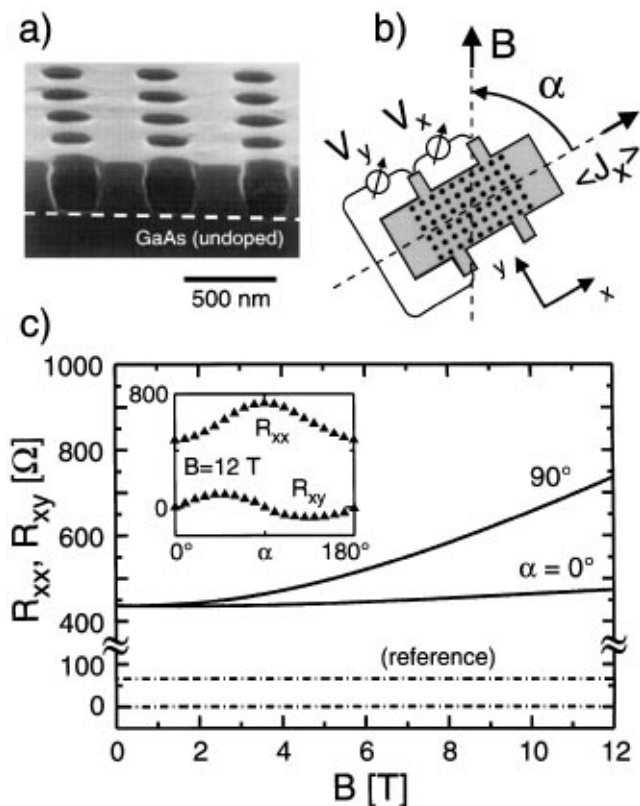
FIG. 1. (a) Electron micrograph of a cleaved GaAs antidot sample with period $a = 500$ nm. The boundary between the n-doped 300 nm thick GaAs layer and the undoped GaAs is marked with a dashed line. (b) Schematic experimental setup for the magnetoresistance measurements. A constant current of 1 μA is applied in the x direction. The Hall bar is rotated *in situ* with respect to the in-plane magnetic field, while the resistance tensor components R_{xx} and R_{xy} are measured in four-terminal geometry. (c) R_{xx} versus $|\mathbf{B}|$ for an antidot sample with $r = 130$ nm for $\alpha = 0°$ and $\alpha = 90°$ (solid lines). Reference data from the unpatterned device are shown as dash-dotted lines (upper trace: R_{xx}; lower trace: R_{xy}). Inset: Full angular dependence of R_{xx} and R_{xy} for the antidot sample at fixed $|\mathbf{B}| = 12$ T. All data were taken at $T = 90$ K.

Figure 1(c) displays characteristic data taken from an antidot sample and the corresponding unpatterned reference film. As expected, R_{xy} of the reference sample is practically zero, while R_{xx} is finite but independent of $|\mathbf{B}|$ and α (to less than 1% at 12 T). By contrast, both R_{xx} and R_{xy} of the antidot device show a striking dependence on α and $|\mathbf{B}|$. R_{xx} exhibits a maximum when $\langle J_x \rangle \perp \mathbf{B}$ and a minimum for $\langle J_x \rangle \parallel \mathbf{B}$, while R_{xy} alternates, having local extrema at $\pi/4$ and $3\pi/4$ [see inset of Fig. 1(c)].

On the left hand side of Fig. 2 polar plots summarize the experimental data for three antidot arrays with different hole diameters. The azimuthal scale corresponds to the angle α while the radial quantity is the normalized resistivity change $\delta\rho_{xx}(|\mathbf{B}|, \alpha)/\rho_0$, shown for $|\mathbf{B}| = 4$, 8, and 12 T, corresponding to $\mu|\mathbf{B}| = 1, 2, 3$, respectively. Here, ρ_0 is the zero-field resistivity of each antidot

sample. For all samples, a positive magnetoresistance can be observed, which depends characteristically on the hole diameter. With decreasing antidot diameter the relative resistance changes become smaller, but more structure appears in the angular dependence. For the smallest holes, with (geometrical) diameter 110 nm, additional local minima appear around 60° and 120°. The experimental data are well reproduced by classical calculations, as shown on the right hand side of Fig. 2 and addressed below.

Angular profiles which follow roughly a $\sin^2\alpha$ law (with α the angle between $\langle \mathbf{J} \rangle$ and $\mathbf{B}$), as in Fig. 2(e), have been reported before, e.g., in semiconductor layers with periodically modulated donor density [4] and in NiSb/InSb systems [5]. However, the richer angular structure, as seen in Fig. 2(a), indicates effects that cannot be accounted for by this earlier work. This angular profile for the sample with the smallest holes is reminiscent of what is observed in pure metals with a noncompact Fermi surface, like copper [13]. However, while the latter is a quantum effect connected with the detailed structure of the Fermi surface, the angular dependence in Fig. 2(a) reflects a nonisotropic resistivity tensor whose origin is entirely classical. Ideally, this could be seen in an experiment where, contrary to ours, the direction of $\langle \mathbf{J} \rangle$ is *fixed* with respect to $\mathbf{B}$ while the antidot lattice is rotated. While this is difficult to implement, it is possible to transform the measured ρ_{xx} and ρ_{xy} values into resistivities $\rho_\perp$ [14] and $\rho_\parallel$, defined with respect to a counterclockwise rotated $x'y'$-coordinate system [see Fig. 1(b) and the top of Fig. 3], where $\langle \mathbf{J} \rangle$ is fixed either perpendicular or parallel to $\mathbf{B}$, respectively. In both the direct experimental and the transformed representations, the antidot lattice is inclined by α with respect to $\mathbf{B}$. For a given
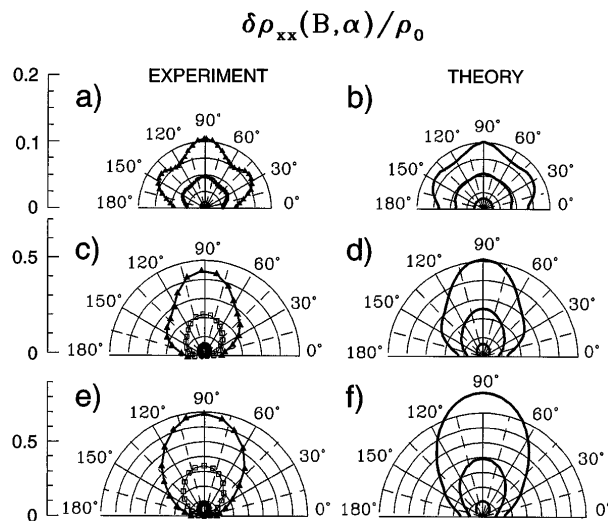
$$\delta\rho_{\mathbf{xx}}(\mathrm{B}, \alpha)/\rho_0$$

FIG. 2. Polar diagrams of $\delta\rho_{xx}(|\mathbf{B}|, \alpha)/\rho_0$ for fixed $|\mathbf{B}| = 4$ (circles), 8 (squares), and 12 T (triangles), and three different *lithographic* antidot radii r of 55 nm (a), 110 nm (c), and 130 nm (e). The calculated traces are obtained for *effective* radii of 73 nm (b), 180 nm (d), and 215 nm (f); the normalized effective thickness of the film was $d/a = 0.45$.
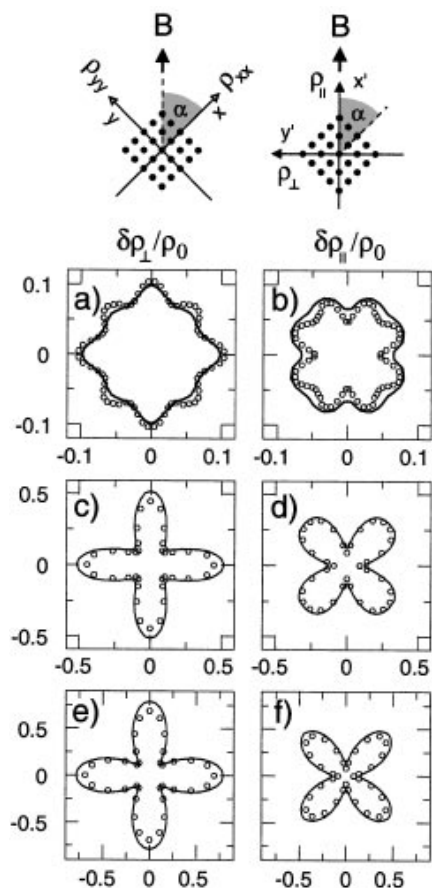
FIG. 3. Polar plots of $\delta\rho_\perp(\mathbf{B})/\rho_0$ and $\delta\rho_\parallel(\mathbf{B})/\rho_0$ for three antidot radii at $|\mathbf{B}| = 12$ T, i.e., $\mu|\mathbf{B}| = 3$. Experimental points are shown as open circles, theoretical fits as full lines. The lithographic antidot radii are $r = 55$ nm (a),(b), 110 nm (c),(d), and 130 nm (e),(f). Fit parameters used in the calculations are the same as for Fig. 2. Top: Sketch of the experimental xy- (left) and rotated $x'y'$-coordinate systems. In experiment, the xy frame (the Hall bar) is rotated with respect to $\mathbf{B}$ while in the transformed $x'y'$ system only the antidot lattice is rotated by α.

angle α the rotation transformation to obtain $\hat{\rho}'$ reads $\hat{\rho}' = \hat{T}(\alpha)\hat{\rho}\hat{T}^{-1}(\alpha)$ with the transformation matrix elements $T_{xx} = T_{yy} = \cos\alpha$, $T_{xy} = -T_{yx} = \sin\alpha$ and the measured resistivity components $\rho_{xy}(\alpha) = \rho_{yx}(\alpha)$ and $\rho_{xx}(\alpha) = \rho_{yy}(\pi/2 - \alpha)$. We thus obtain the diagonal elements $\rho_\parallel \equiv \rho'_{x'x'}$ and $\rho_\perp \equiv \rho'_{y'y'}$. The normalized resistivities $\delta\rho_\perp/\rho_0$ and $\delta\rho_\parallel/\rho_0$, displayed in Figs. 3(a)–3(f), exhibit a characteristic cross ($\delta\rho_\perp$) or cloverleaf ($\delta\rho_\parallel$) shape with respect to the lattice axes. Again, the sample with the smallest holes [Figs. 3(a) and 3(b)] shows additional angular structure. Note that, even for the sample with the largest hole diameter [Figs. 3(e) and 3(f)], the anisotropy is clearly manifested in this representation, in contrast with a random distribution of voids, where both $\rho_\perp$ and $\rho_\parallel$ would be *entirely isotropic*.

The experimental data in Figs. 3 and 2 are in striking agreement with calculated traces, which result from a clas-

sical calculation based upon the current continuity equation $\nabla \cdot [\hat{\sigma}(\mathbf{r})\nabla\phi(\mathbf{r})] = 0$ for the local electric potential $\phi(\mathbf{r})$, using the local free-electron conductivity tensor $\hat{\sigma}$. The detailed technique which was developed for performing that calculation is described elsewhere [9–11].

In order to compare our data with calculations we have to take into account depletion regions at free surfaces and at the doped or undoped GaAs interface, which increase the hole diameters and reduce the film thickness. We estimate a depletion length of $l_d \approx 25$ nm around the holes and an effective GaAs film thickness of $d \approx 240$ nm. To obtain best agreement with experiment we had to use effective radii which, for the larger holes [plots in Figs. 2(c)–2(f) and 3(c)–3(f)], exceed by typically 35% the sum of
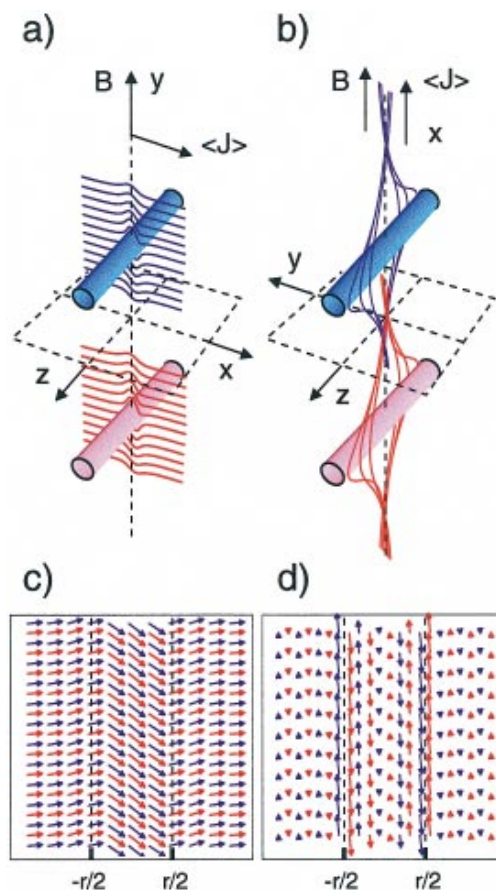
FIG. 4(color). (a),(b) Calculated current lines in the vicinity of a pair of cylindrical antidots for $\mathbf{B}\perp\langle\mathbf{J}\rangle$ and $\mathbf{B}\parallel\langle\mathbf{J}\rangle$, corresponding to $\alpha = 90°$ and $\alpha = 0°$ in the xy-coordinate system of the experiment. Blue distortions arise solely from the blue cylinder, likewise for red. Note that also in (a) the current lines experience significant shifts along the cylinder axes, clearly visible in the projection plots below. (c),(d) Projections of the current vector fields in the symmetry plane between the blue and red cylinders onto that plane. The area between the vertical dashed lines indicates the projection of the cylinders (above and below) onto the plane. The calculations were performed for $\mu|\mathbf{B}| = 10$.

149

lithographic radius and l_d. This could be due to the gradual change of the carrier density between the holes in contrast to the hard wall inclusions used in the model.

Some aspects of the detailed calculations can be presented in a simple picture illustrating how interaction between current distortions generated by neighboring obstacles leads to the anisotropy. First consider the distortion of a current flow (in the x direction) caused by an isolated obstacle, e.g., the blue cylinder in Fig. 4(a). Those distortions are essentially limited to a slab-shaped volume of length proportional to $\mu|\mathbf{B}|$ in the direction of $\pm\mathbf{B}$ [8] ("geometrical shadow" of the cylinder). The "bumps" in the current flow pattern, which have pronounced components also along the $\pm z$ directions, lead to enhanced dissipation proportional to $|\mathbf{B}|$ if $\mu|\mathbf{B}| \gg 1$. Interaction effects arise when the flow patterns of two adjacent inclusions start to overlap. A significant anisotropy of the resistance was predicted to appear for $\mu|\mathbf{B}| > 1$ [10,11].

The interaction can be analyzed qualitatively by considering the superposition of distortion patterns from two isolated obstacles. To that end we show, in Figs. 4(a) and 4(b), the current flow around two cylinders for $\langle\mathbf{J}\rangle\perp\mathbf{B}$ and $\langle\mathbf{J}\rangle \parallel \mathbf{B}$, where the distortion pattern around each cylinder was calculated neglecting the influence of the other. The orientation of the coordinate system in Fig. 4 corresponds to $\alpha = 90°$ (a) and $\alpha = 0°$ (b) in the experiment. Note, however, that the figures also represent $\rho_\perp$ (a) and $\rho_\parallel$ (b) for $\alpha = j\pi/2$ with $j = 0, 1, 2\dots$. In terms of the transformed representation these angles are all equivalent for a square lattice. Figures 4(c) and 4(d) show the two flow fields [corresponding to Figs. 4(a) and 4(b)] projected onto the symmetry plane (perpendicular to $\mathbf{B}$) halfway between the cylinders. The total in-plane current is obtained by adding the two vector fields. Clearly, in Fig. 4(c) there is a perfect reinforcement while in Fig. 4(d) there is a perfect cancellation of the two distortion patterns. This corresponds, for $\alpha = j\pi/2$, to a maximum in $\rho_\perp$ and a minimum in $\rho_\parallel$ [15]. When $\mathbf{B}$ is tilted away from the cylinder-axes plane, i.e., α is changed, the amplification and cancellation of the current distortions become less perfect, resulting in a reduced $\rho_\perp$ and enhanced $\rho_\parallel$.

For holes with smaller radii, the onset of anisotropy occurs at higher $\mathbf{B}$. On the other hand, for a radius which is small compared to the period of the antidot lattice the interference of patterns from nearest neighbors along additional directions, e.g., the 45° direction (see also top of Fig. 3) becomes possible. This is due to the fact that the geometrical shadow can now reach a neighboring void along the diagonal of the square lattice, if the diameter of the inclusions is not too large. We therefore expect to find an additional maximum for $\rho_\perp$ and a minimum for $\rho_\parallel$ along the 45° directions [10]. These

features are clearly evident in Figs. 3(a) and 3(b). A more detailed, quantitative discussion of the interactions between current distortions from different obstacles and the local dissipation rate can be found in Refs. [10,16].

Finally, we note that the current distortions are *three dimensional*. They exhibit a nonvanishing component *along* the cylinder axes [see Figs. 4(a) and 4(b)]. Decreasing the film thickness reduces this component, and hence the anisotropy as well as the magnitude of the magnetoresistance [11]. For a strictly two-dimensional system there would be no magnetoresistance.

[1] For a review, see A. B. Pippard, *Magnetoresistance in Metals* (Cambridge University Press, Cambridge, England, 1989).

[2] G. J. C. L. Bruls, J. Brass, A. P. van Gelder, H. van Kempen, and P. Wyder, Phys. Rev. Lett. **46**, 553 (1981).

[3] C. J. Beers, J. C. M. van Dongen, H. van Kempen, and P. Wyder, Phys. Rev. Lett. **40**, 1194 (1978).

[4] H. Weiss, in *Semiconductors and Semimetals,* edited by R. K. Willardson and A. C. Beer (Academic, New York, 1966), Vol. 1, and references therein.

[5] H. Weiss and M. Wilhelm, Z. Phys. **176**, 399 (1963).

[6] Note that $\int_V dV\{[\mathbf{J}(\mathbf{r}) - \langle\mathbf{J}\rangle] \cdot \hat{\rho} \cdot [\mathbf{J}(\mathbf{r}) - \langle\mathbf{J}\rangle]\} = \int_V dV\, \mathbf{J}(\mathbf{r}) \cdot \mathbf{E}(\mathbf{r}) - V\langle\mathbf{J}\rangle \cdot \hat{\rho} \cdot \langle\mathbf{J}\rangle \geq 0$ holds, if the local form of Ohm's law, $\mathbf{E}(\mathbf{r}) = \hat{\rho} \cdot \mathbf{J}(\mathbf{r})$ remains valid. Here, $\hat{\rho}$ is the *local* resistivity in the conductive medium.

[7] C. Herring, J. Appl. Phys. **31**, 1939 (1960).

[8] J. B. Sampsell and J. C. Garland, Phys. Rev. B **13**, 583 (1976).

[9] Y. M. Strelniker and D. J. Bergman, Phys. Rev. B **50**, 14 001 (1994).

[10] D. J. Bergman and Y. M. Strelniker, Phys. Rev. B **49**, 16 256 (1994).

[11] D. J. Bergman and Y. M. Strelniker, Phys. Rev. B **51**, 13 845 (1995).

[12] D. Weiss, P. Grambow, K. v. Klitzing, A. Menschig, and G. Weimann, Appl. Phys. Lett. **58**, 2960 (1991).

[13] J. R. Klauder and J. E. Kunzler, in *The Fermi Surface,* edited by W. A. Harrison and M. B. Webb (Wiley, New York, 1960).

[14] In the notation of Refs. [10,11,16] our $\rho_\perp$ corresponds to $\tilde{\rho}_\perp$ and vice versa.

[15] The energy dissipation is dominated by distortions *in the plane perpendicular to* $\mathbf{B}$, see Ref. [16].

[16] Y. M. Strelniker and D. J. Bergman, Phys. Rev. B **53**, 11 051 (1996).